Journal of Materials Science: Materials in Electronics (2020) 31:7067–7075
https://doi.org/10.1007/s10854-020-03276-z

Study on ion migration characteristics and aging stability of $MgTiO_3$ and $LaTiO_3$ composites ceramic for high temperature negative temperature coefficient ceramics

Jing Yang[1] · Huimin Zhang[2,3] · Xu Sang[2] · Aimin Chang[2,3] · Zhi Su[1]

Received: 24 December 2019 / Accepted: 19 March 2020 / Published online: 27 March 2020

Abstract

It was found for the first time that high temperature negative temperature coefficient (NTC) composites ceramic of $La_{1-x}Mg_xTiO_3$ ($x=0.1$, 0.3, 0.5, 0.7, 0.9) have been prepared by the solid-state reaction method sintered at 1400 °C. The effects of $MgTiO_3$ and $LaTiO_3$ composites on the structure, electrical properties and stability of the sintered ceramic samples were characterized by thermogravimetry–differential scanning calorimetry (TG–DSC), X-ray diffraction (XRD), scanning electron microscope (SEM), energy-dispersive spectroscopy (EDS), Mapping, X-ray photoelectron spectroscopy analysis. XRD patterns analysis has revealed that for $La_{1-x}Mg_xTiO_3$ ($x=0.1$, 0.3, 0.5, 0.7, 0.9) the major phases presents in the calcined bodies are double perovskites the $LaTiO_3$ phase and the $MgTiO_3$ phase. The SEM images have exhibited that as the mole fraction of Mg^{2+} from 0.1 to 0.9, the grain size of the $MgTiO_3$ ceramics increases from ca. 1.77 to 5.99 μm and $LaTiO_3$ ceramics decreases from ca. 2.83 to 1.53 μm. X-ray photoelectron spectroscopy prove the Ti^{3+} and Ti^{4+} ions on lattice sites, which result in hopping conduction. The presence of the Ti^{3+} and Ti^{4+} ions is one of the significant factors that affect the electrical conductivity of $La_{1-x}Mg_xTiO_3$ composites ceramic. The ρ_{400} and $B_{400/1200}$ values are in the range of 14,693.137–65,659.809 Ω·cm and 7785.270–24,948.100 K, respectively. The $La_{1-x}Mg_xTiO_3$ materials could be used as potential candidates for high temperature range from 400 to 1200 °C thermistors applications. The resistance variation ($\Delta R/R_0$) was < 2% and the minimum value (0.1%) was obtained for aging at 1100 °C at 800 h. The aim of this work was exploring new composite ceramics materials, which could be used as higher temperature zones.

1 Introduction

Negative temperature coefficient (NTC) thermistors are thermally sensitive resistors whose resistance decreases with increasing temperature [1–4]. NTC thermistor can be divided into: (1) low temperature thermistor (< − 173 °C); (2) middle temperature thermistor (− 60 ≤ 300 °C); (3) high temperature thermistor (> 300 °C). High temperature thermistor is mainly used for high temperature measurement; temperature control; temperature compensation. With the rapid development of science and technology, this function of high temperature thermistor is needed in automobile electronics, military industry, aerospace and other fields. At present, platinum resistance temperature sensor is mainly used to take temperature in high temperature and wide temperature region, but it is difficult to realize the linearization of resistance temperature above 850 °C, the measurement accuracy can not be guaranteed, and the price of raw materials is expensive. Due to the NTC thermistor material has good stability, high sensitivity and low

✉ Huimin Zhang
zhanghm@ms.xjb.ac.cn

✉ Aimin Chang
changam@ms.xjb.ac.cn

✉ Zhi Su
suzhixj@sina.com

[1] College of Chemistry and Chemical Engineering, Xinjiang Normal University, Ürümqi, China

[2] Key Laboratory of Functional Materials and Devices for Special Environments of CAS, Xinjiang Key Laboratory of Electronic Information Materials and Devices, Xinjiang Technical Institute of Physics and Chemistry of CAS, Ürümqi, China

[3] Center of Materials Science and Optoelectronics Engineering, University of Chinese Academy of Sciences, Beijing 100049, China

price, so it is widely used in temperature measurement and control, surge current suppression and a temperature compensation [5, 6]. Traditionally, most NTC materials are Ni- and Mn-based spinel oxides, but the application of spinel NTC thermistors is commonly limited to temperatures below approximately 200 °C [7]. Compared to the spinel-type material, the perovskite-type compound ABO_3 has structure is relatively close, the properties are relatively stable at higher temperatures and aging resistance. Moreover, the cations A site and B site in perovskite-type compound ABO_3 are fixed at the lattice position regardless of temperature. Therefore, the application of perovskite-type composite oxides is very wide, including magnetism [8, 9], giant magnetic resistance [10], solid oxide fuel cells [11, 12], transducer sensors [13, 14], multifunctional conductive ceramic materials [15, 16], catalysis [17, 18], and photocatalysis fields [19, 20]. According to reports, many authors have prepared single-phase, two-phase composite, and multiphase composite perovskite materials through different material systems, preparation methods, test characterization methods and related mechanisms for dielectric and high temperature NTC thermistors applications [21–24]. Subsequently, research on high temperature NTC thermistor materials has increasingly focused on the perovskite structure materials in recent years. The materials composed of rare metal oxides such as Y_2O_3, La_2O_3 and Mn_2O_3 with the perovskite structure, Al_2O_3, Zr_2O_3 and other high temperature solid solution phases have been turned up to have good wide temperature performance. The perovskite compounds have also been studied for the NTC thermistors.

Among in all kinds of oxides, titanium oxides with pseudo-cubic perovskite structure (titanate with uniform $ATiO_3$ or $RTiO_3$ chemical formula) have some special physical properties [25]. It is usually used in electro-optic, piezoelectric, dielectric, ferroelectric, photocatalysis and other applications [26, 27]. Perovskite materials can be doped with different cations at A sites or B sites in order to customize the properties of the materials. Bradha et al. has studied the conductive properties of $LaTiO_3$ doped with Sc ion. The same Sc ion doping content in different $LaTiO_3$ properties doping, oxygen vacancy can be produced in the lattice to allow mixed ions and electron conduction in perovskite [28]. Most commonly, divalent cationic doping $LaTiO_3$ perovskite structure materials on NTC thermistors have been reported, such as Cu^{2+} [29], Ba^{2+} [30], Ca^{2+} [31], Sr^{2+} [32, 33] etc. However, the Mg^{2+} doping of $LaTiO_3$ perovskite structure materials form a composite structure has been never reported. According to the reports in the literatures [34], (1) MgO can form a favorable solid solution of the cubic perovskite structure with $BaCO_3$, TiO_2, and La_2O_3 at high temperature; (2) Mg^{2+} based on perovskite structure, occupying the A site, suppress the separation of the secondary phase, which may enhance aging stability of material; (3) the ratio of Ti^{3+}/Ti^{4+} can be more precise regulation stabilized by the introduction of Mg^{2+}.

Therefore, in this paper, high temperature negative temperature coefficient ceramic of $La_{1-x}Mg_xTiO_3$ composites ceramic samples were prepared by divalent cationic doping Mg^{2+} form a composite structure by the solid-state reaction method.

The ion migration characteristics and aging stability of $MgTiO_3$ and $LaTiO_3$ composites for high temperature NTC composites ceramic $La_{1-x}Mg_xTiO_3$ are obtained by its morphology and structural analysis.

2 Experimental procedure

The $La_{1-x}Mg_xTiO_3$ powders were synthesized by solid-state reaction method. High-purity lanthanum oxide (99.99%), titanium dioxide (99.99%) and magnesium oxide (99.99%) were used as initial raw materials. The initial raw materials were weighed according to the composition of $La_xMg_{1-x}TiO_3$ ($x=0.1, 0.3, 0.5, 0.7, 0.9$) placed in a ball mill jar, using agate balls as grinding media and ethanol as the dispersant ball milling, drying at 120 °C and grinding, calcined at 1200 °C for 2 h. The calcined powders were then ground in mortar for 8 h. Afterward, the powders were pressed at 180 MPa into Φ10 × 1.2 mm cylindrical disks. The pressed disks were sintered in the temperature of 1400 °C for 7 h in air. The silver paste was coated on both surfaces of sintered pellets as electrode.

The material powder optimal calcination temperature of the $La_{1-x}Mg_xTiO_3$ ($x=0.1, 0.3, 0.5, 0.7, 0.9$) powders were analyzed by TG–DSC (Netzsch STA449F). The phase structure of the sintered ceramic samples was investigated by X-ray diffraction (XRD; Bruker D8-ADVANCE, Cu Kα

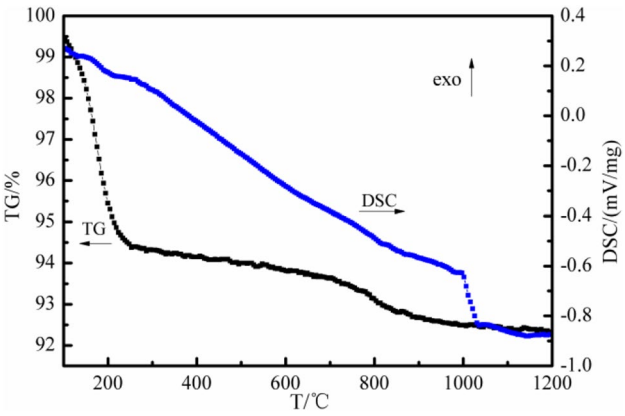

Fig. 1 TG–DSC curves for the $La_{0.9}Mg_{0.1}TiO_3$ powders

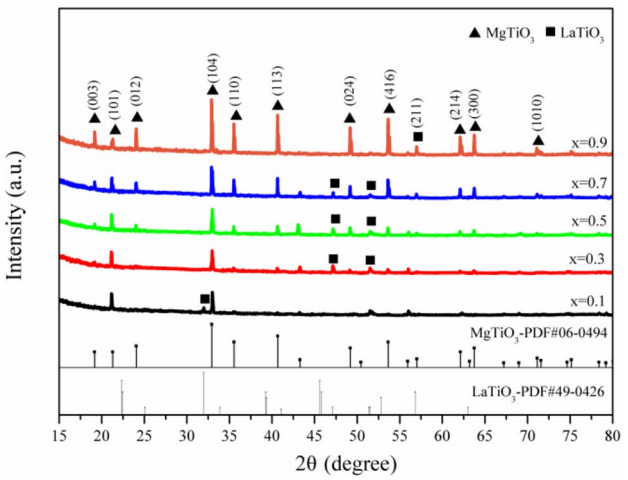

Fig. 2 XRD patterns of composites sintered ceramic samples of $La_{1-x}Mg_xTiO_3$ sintered at 1400 °C: ($x = 0.1, 0.3, 0.5, 0.7, 0.9$)

radiation, $\lambda = 0.15418$ nm, 0.01°/s). The microstructure of the sintered ceramic samples were observed the scanning electron microscope (SEM: LEO1430VP, Germany) and energy-dispersive spectroscopy (EDS). X-ray photoelectron spectroscopy (XPS: Thermo Fisher, ESCALAB 250) was used to analyze the chemical states of the sintered ceramics. The electrical resistance of the sintered ceramic samples was measured from 400 to 1200 °C, using digital multimeter (Hewlett Packard, 34401A). Aging was conducted by keeping the samples in an oven at 1100 °C in air for 800 h. Aging is defined by $\Delta R/R_0 = (R - R_0)/R_0$, where R_0 and R are the resistance at 1100 °C before and after aging, respectively.

3 Results and discussion

Figure 1 shows the simultaneous TG–DSC curves of the $La_{0.9}Mg_{0.1}TiO_3$ powders under air atmosphere. The curves described the weight loss profiles that occur in several stages. From room temperature to 238 °C, the weight loss of TG curve is 5.5%, which is associated with the evaporation of the absorbed water, the removal of the crystallized water. The second stage in the range of 300–1000 °C with weight loss is 1.5% that attributed to the oxygen loss and formation of perovskite phase and the structure variation in TiO_6 octahedron under higher calcination temperatures [35]. This indicates that all powders can be calcined at 1000 °C for 2 h to obtain a perovskite phase.

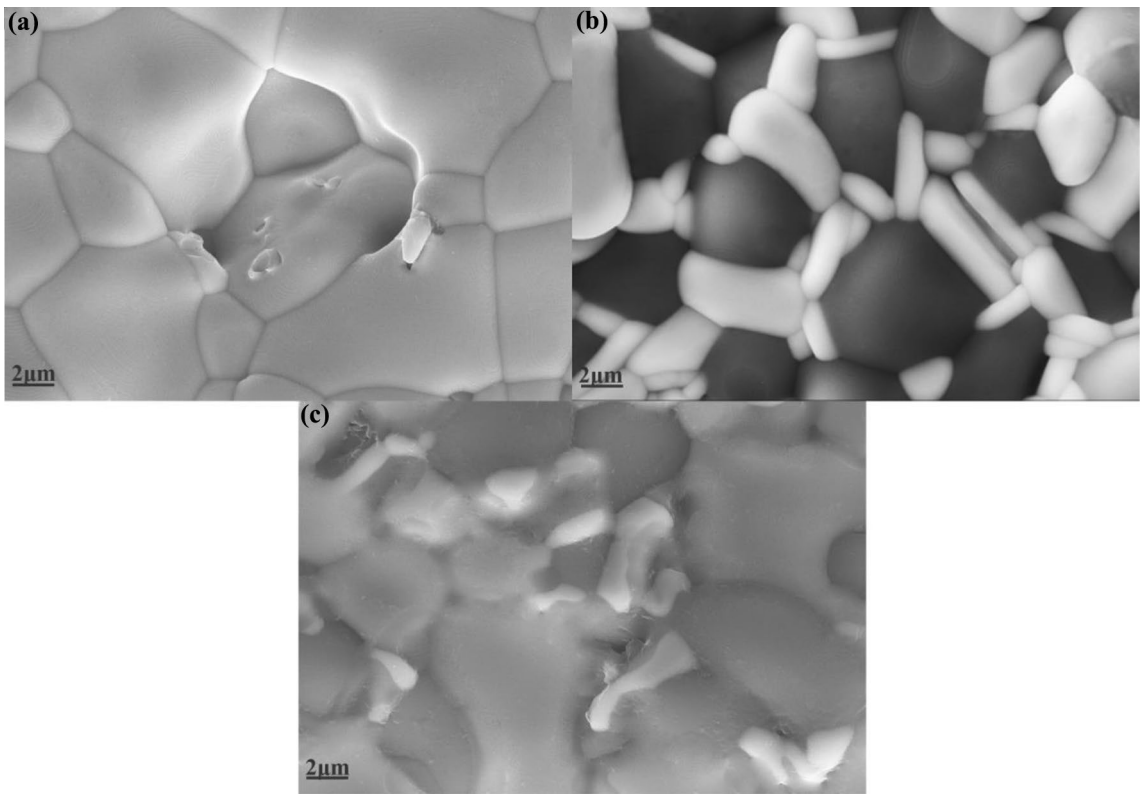

Fig. 3 SEM micrographs of the $La_{0.3}Mg_{0.7}TiO_3$ composites sintered ceramic samples: **a** sintered at 1350 °C, **b** sintered at 1400 °C, and **c** sintered at 1450 °C

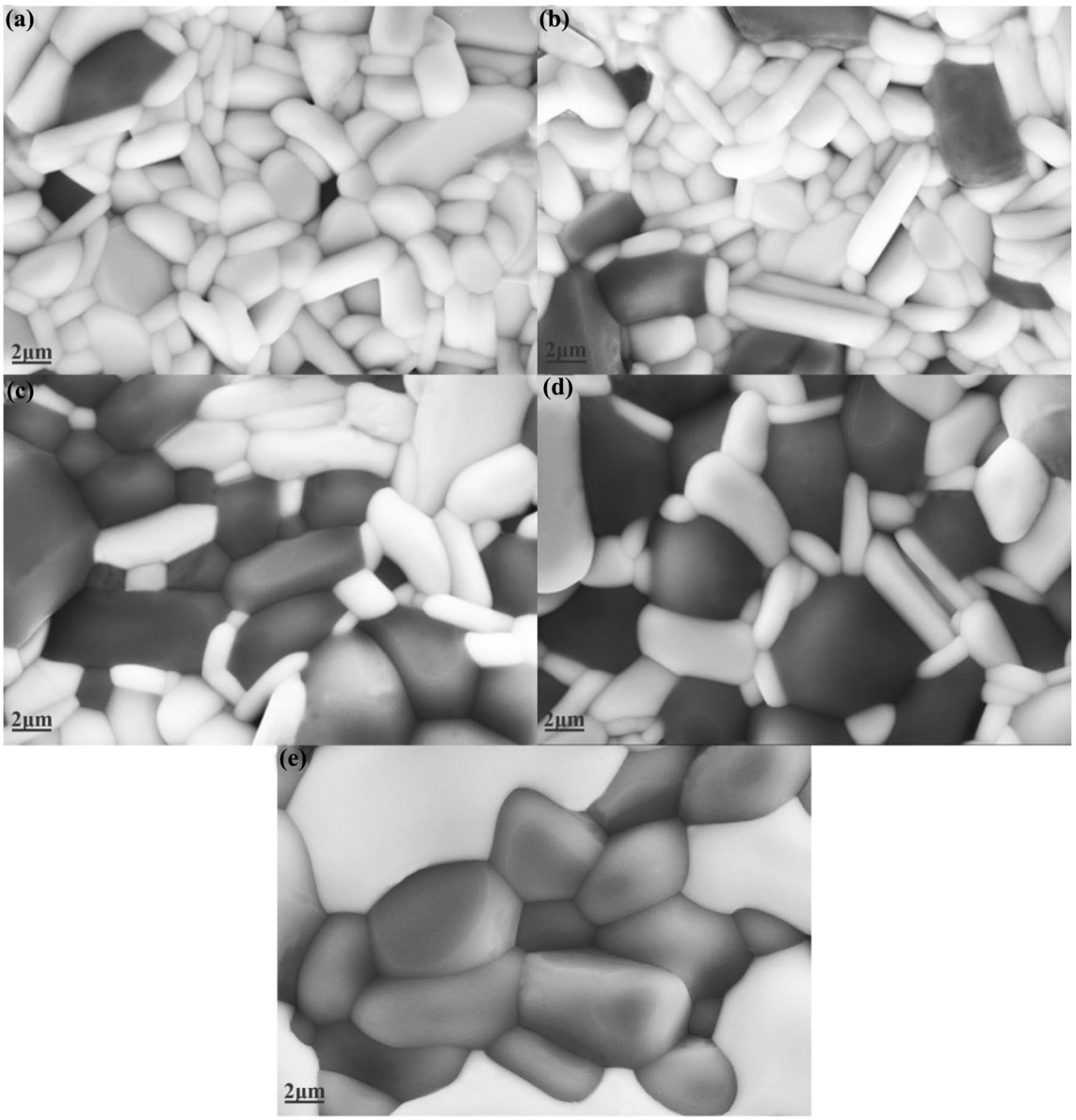

Fig. 4 SEM micrographs of the $La_{1-x}Mg_xTiO_3$ composites sintered ceramic samples (sintered at 1400 °C): **a** $x=0.1$, **b** $x=0.3$, **c** $x=0.5$, **d** $x=0.7$, and **e** $x=0.9$

Figure 2 shows the indexed X-ray diffraction patterns of $La_{1-x}Mg_xTiO_3$ ($x=0.1$, 0.3, 0.5, 0.7, 0.9) composites sintered ceramic samples sintered at 1400 °C for 7 h. A system with rhombohedral-structured $MgTiO_3$ (JCPDS#06-0494) as main phase that orthorhombic-structured $LaTiO_3$ (JCPDS#49-0426) as secondary phases. It was observed that with increase in Mg^{2+} content, intensity of $MgTiO_3$ diffraction peaks increased and that of $LaTiO_3$ decreased. It was also observed that the $MgTiO_3$ diffraction peaks shifted towards lower 2θ values with an increase in Mg^{2+} content as expected, which could be attributed to larger ionic radii of La^{3+} (0.106 pm) than that of Mg^{2+} (0.065 nm). The formation of multiple phases in the present system could be due to structural differences in compounds.

Figure 3a–c shows the SEM micrographs of $La_{0.3}Mg_{0.7}TiO_3$ composites sintered ceramic samples at different sintering temperatures (1350 °C, 1400 °C, 1450 °C). It can be seen from the image that when the sintering temperature is 1350 °C, the $La_{0.3}Mg_{0.7}TiO_3$ composites sintered ceramic samples grain development is relatively complete and the grain sizes ranged from 6.50 to 10.96 μm, but there are tiny holes between the grain boundaries, and the compactness is not good. When the sintering temperature is 1450 °C, the $La_{0.3}Mg_{0.7}TiO_3$ composites sintered ceramic samples grain development is incomplete and the grain

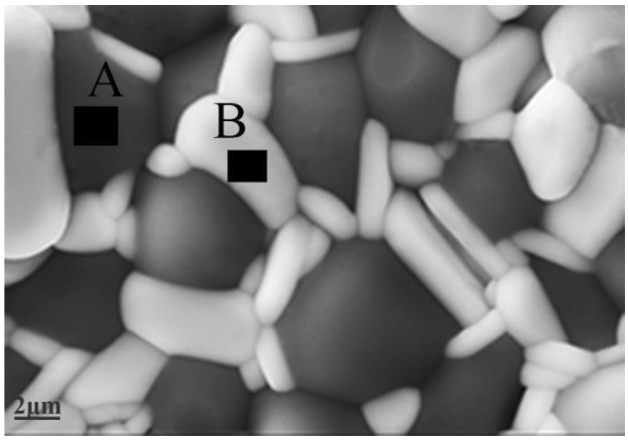

Fig. 5 SEM micrograph of the $La_{0.3}Mg_{0.7}TiO_3$ composites sintered ceramic samples

Table 1 EDS for the atomic and weight percentage of $La_{0.3}Mg_{0.7}TiO_3$ composites sintered ceramic samples: various elements (A, B, are sintered at 1400 °C)

$La_{0.3}Mg_{0.7}TiO_3$	Element		
	La	Mg	Ti
A			
Wt%	0	9.94	50.25
At.%	0	10.37	26.59
B			
Wt%	47.40	0	21.87
At.%	12.54	0	16.77

boundary does appear to be excessively burnt. When the sintering temperature is 1400 °C, the $La_{0.3}Mg_{0.7}TiO_3$ composites sintered ceramic samples grain development is complete, the grain boundary is obvious, the grain size tends to be uniform and the grain sizes ranged from 2.20 to 6.13 μm, the arrangement is dense, and there is no hole. Therefore, the optimum sintering temperature of $La_{0.3}Mg_{0.7}TiO_3$ composites sintered ceramic samples were selected at 1400 °C.

Figure 4a–e shows the SEM images of $La_{1-x}Mg_xTiO_3$ ($x=0.1, 0.3, 0.5, 0.7, 0.9$) composites sintered ceramic samples at 1400 °C. It can be seen that all of the composites sintered ceramic samples were highly dense and grain development is complete. The composites sintered ceramic samples contain two kinds of grains of different sizes, the $LaTiO_3$ phase and the $MgTiO_3$ phase, respectively. In addition, it can be seen that the introduction of MgO phase affects the microstructure of $La_{1-x}Mg_xTiO_3$ composites sintered ceramic samples phase to a great extent. With the increase of Mg^{2+} content, the average grain of $MgTiO_3$ phase increases, and the grain sizes ranged from 1.77 to 5.99 μm and the average grain of $LaTiO_3$ phase decreases, the grain sizes ranged from 2.83 to 1.53 μm. When the doping Mg^{2+} amount $x=0.9$ that extended contact to high temperature has resulted in agglomeration and fusion of the particles which appear as $LaTiO_3$ phase grains in microstructural images. The results show that the appearance of $MgTiO_3$ phase in the $La_{1-x}Mg_xTiO_3$ ($x=0.1, 0.3, 0.5, 0.7, 0.9$) composites sintered ceramic samples can inhibit the grain growth of $LaTiO_3$ phase.

Figure 5 shows the SEM image of $La_{0.3}Mg_{0.7}TiO_3$ composites sintered ceramic samples at 1400 °C. The two forms of light and dark can be seen obviously, which indicates the different phases of the two composite ceramics. The compositions taken from the brighter and darker grains of polished and thermally etched surfaces for the $La_{0.3}Mg_{0.7}TiO_3$ composites sintered ceramic samples were qualitatively identified by EDS, as shown in Table 1, respectively. It can be seen that two tone contrasts were observed in Fig. 5, which indicates the two different phases of the sintered ceramic samples.

Figure 6 is the surface SEM diagram of $La_{0.3}Mg_{0.7}TiO_3$ composites sintered ceramic samples sheet and its

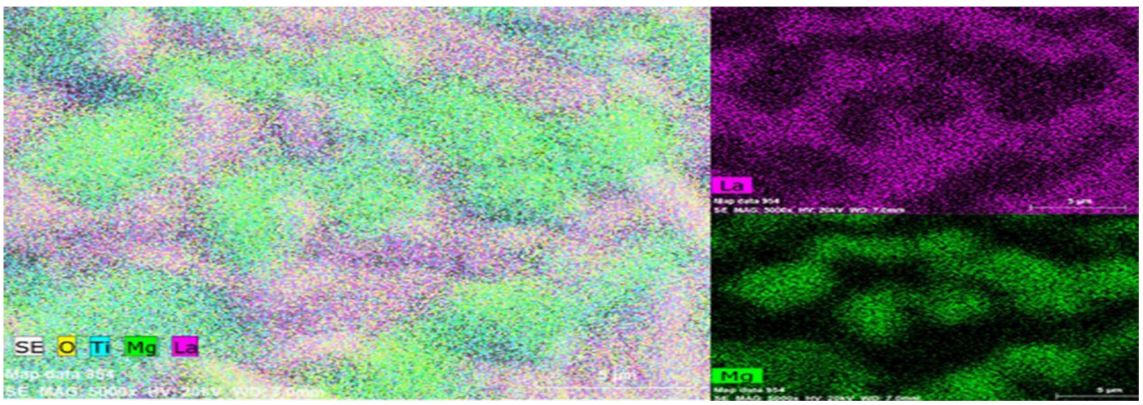

Fig. 6 Mapping of $La_{0.3}Mg_{0.7}TiO_3$ composites sintered ceramic samples

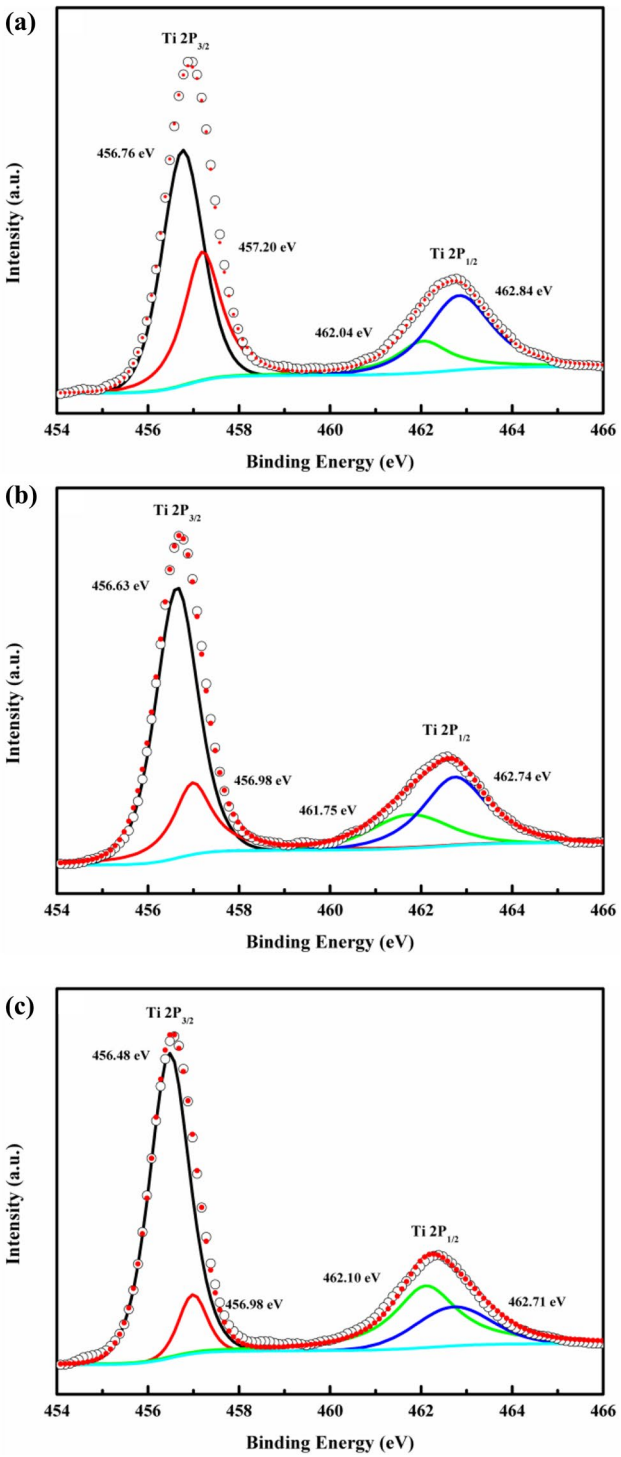

Fig. 7 Ti 2p XPS spectra collected for $La_{1-x}Mg_xTiO_3$ composites sintered ceramic samples at 1400 °C: **a** $x=0.5$, **b** $x=0.7$, and **c** $x=0.9$

corresponding mapping map of each element. Where the: is the La element, is the Mg element. When the molar ratio of $LaTiO_3$ to $MgTiO_3$ is 3:7, the distribution of $LaTiO_3$ and $MgTiO_3$ is uniform. La elements are distributed in the position of $LaTiO_3$ phase, Mg elements are distributed in the position of $MgTiO_3$ phase, and $LaTiO_3$ and $MgTiO_3$ elements complement each other in SEM image.

To confirm the mixed-valent Ti^{3+}/Ti^{4+} of Ti, that by obtained the XPS spectra of the Ti 2p regions for the $La_{0.5}Mg_{0.5}TiO_3$, $La_{0.3}Mg_{0.7}TiO_3$ and $La_{0.1}Mg_{0.9}TiO_3$ composites sintered ceramic samples. As shown in Fig. 7, the XPS spectra data were analyzed in detail by Gaussian–Lorentzian curve fitting. All asymmetrical 2p peaks for Ti can be split into two peaks through the Gaussian–Lorentzian curve fitting, indicating the co-existence of Ti^{3+}/Ti^{4+} in $La_{0.5}Mg_{0.5}TiO_3$, $La_{0.3}Mg_{0.7}TiO_3$ and $La_{0.1}Mg_{0.9}TiO_3$. Fitting parameters, such as the area ratios deduced from the fitting peaks, are listed in detail in Table 2. The XPS results presenting herein are in agreement with those by Walle et al. [36]. Examination of the data in Table 2 clearly shows that the peak-area ratios representing the atomic ratio of Ti^{3+}/Ti^{4+} change with the Mg^{2+} compound level. The Ti^{3+} to Ti^{4+} area ratios for the $La_{0.5}Mg_{0.5}TiO_3$, $La_{0.3}Mg_{0.7}TiO_3$ and $La_{0.1}Mg_{0.9}TiO_3$ are 7.5043, 3.0020 and 1.7544, respectively.

The relationship between the natural logarithm of the resistivity ($\ln\rho$) and the reciprocal of the absolute temperature ($1000/T$) for the $La_{1-x}Mg_xTiO_3$ ($x=0.1$, 0.3, 0.5, 0.7, 0.9) NTC composites ceramic samples was obtained, as shown in Fig. 8. Particularly, this figure reveals that the resistivity increases as the composite Mg^{2+} content increases. This result can be explained as follows. The charge compensation resulting from the Mg^{2+} substitution for Ti^{3+} is responsible for the increased ionic conductivity. According to the principle of conservation of charge, in $LaTiO_3$, Ti ions behave as positive trivalent. Due to the doping of Mg^{2+}, $MgTiO_3$ is formed, and Ti ions exhibit positive tetravalent. As the content of Mg^{2+} increases, when La^{3+} in $LaTiO_3$ is partially replaced by Mg^{2+}, due to the charge compensation, part of Ti^{3+} becomes Ti^{4+}, in the form of $Ti^{3+} - e^- \rightarrow Ti^{4+}$, which leads to an increase in the concentration of Ti^{4+}, increase of ion specific concentration of Ti^{4+}/Ti^{3+}, which increases the resistivity of the material.

The energy and $B_{400/1200}$ constant of the $La_{1-x}Mg_xTiO_3$ ($x=0.1$, 0.3, 0.5, 0.7, 0.9) NTC composites ceramic are listed in Table 3, together with the resistivity at 400 °C and 1200 °C. The values of ρ_{400}, $B_{400/1200}$ constant, and

Table 2 XPS fitting parameters of the $La_{0.5}Mg_{0.5}TiO_3$, $La_{0.3}Mg_{0.7}TiO_3$ and $La_{0.1}Mg_{0.9}TiO_3$ composites sintered ceramic samples

x	La^{3+}	Mg^{2+}	Ti^{3+}	Ti^{4+}	Ti^{3+}/Ti^{4+}	Ti^{3+}/Ti^{4+} (aging)
0.5	0.3458	0.0617	0.8824	0.1176	7.5043	1.4877
0.7	0.2663	0.0817	0.7501	0.2499	3.0020	6.3528
0.9	0.2085	0.0841	0.6369	0.3631	1.7544	15.5168

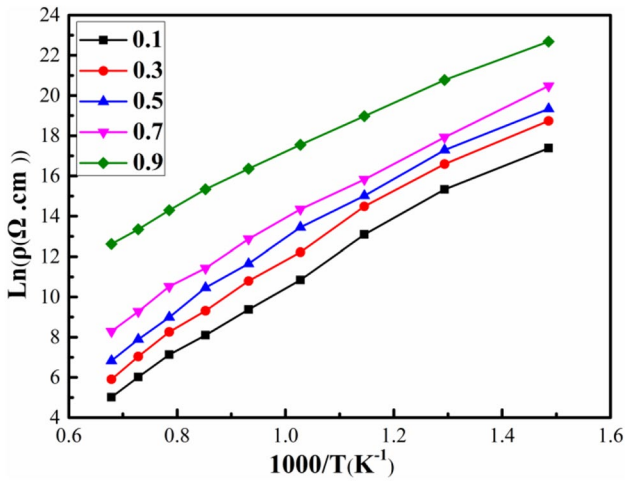

Fig. 8 Relationship between lnρ and 1000/T (K^{-1}) for the $La_{1-x}Mg_xTiO_3$ (x=0.1, 0.3, 0.5, 0.7, 0.9) NTC composites ceramics samples

Table 3 Resistivity at a temperature of 400 °C (ρ_{400}), thermal constant ($B_{400/1200}$) and activation energy for the $La_{1-x}Mg_xTiO_3$ (x=0.1, 0.3, 0.5, 0.7, 0.9) NTC composites ceramic samples

x	ρ_{400} (Ω cm)	ρ_{1200} (Ω cm)	$B_{400/1200}$	E_a (eV)
0.1	14,693.137	931.639	7785.270	0.6711
0.3	20,035.297	1114.798	18,802.727	1.6201
0.5	25,749.534	2288.044	20,400.505	1.7603
0.7	50,307.814	3729.128	21,825.105	1.8807
0.9	65,659.809	5621.844	24,948.100	2.1499

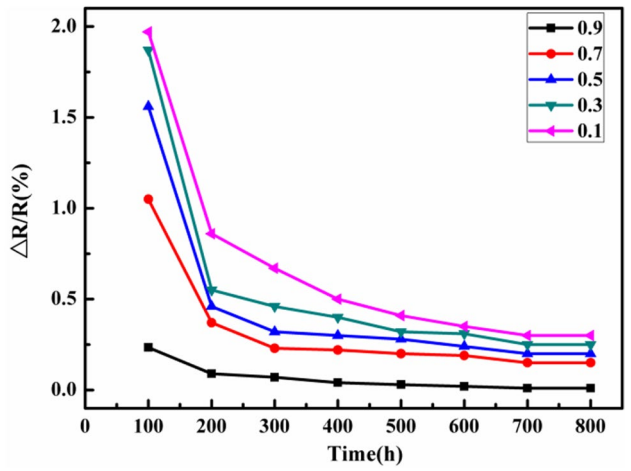

Fig. 9 Aging coefficient $\Delta R/R_0$ after 800 h aging at 1100 °C as a function of Mg^{2+} content x for the $La_{1-x}Mg_xTiO_3$ (x=0.1, 0.3, 0.5, 0.7, 0.9) NTC composites ceramic samples

activation energy of the NTC composites ceramic samples with different compositions are 14,693.14–65,659.81 Ω cm, 7785.270–24,948.100 K, and 0.6711–2.1499 eV, respectively.

The aging coefficient ($\Delta R/R_0$) of Mg^{2+} content for the $La_{1-x}Mg_xTiO_3$ (x=0.1, 0.3, 0.5, 0.7, 0.9) NTC composites ceramic samples after heat treatment 800 h at 1100 °C is shown in Fig. 9. The plots present that the aging at 1100 °C of the aging coefficient ($\Delta R/R_0$) of these composites were 0.1–2% for the time period of 800 h. It is also seen from the Fig. 9 that when the doping Mg^{2+} amount is x=0.1, the drift rate of resistance is large, about 2%, and after aging for 500 h, the aging rate is gradually stabilized. When the doping Mg^{2+} amount is x=0.9, the resistance drift rate is small, about 0.25%, and the resistance drift rate tends to be stable at 400 h. The decrease in $\Delta R/R_0$ of samples results from the variations of the cationic vacancies in the aging process. These behaviors should be ascribed to the microstructural change during aging. The SEM of fracture the $La_{1-x}Mg_xTiO_3$ (x=0.5, 0.7, 0.9) NTC composites ceramic samples aging 800 h at 1100 °C are shown in Fig. 10. In Fig. 10a $La_{0.5}Mg_{0.5}TiO_3$ and Fig. 10b $La_{0.3}Mg_{0.7}TiO_3$ NTC composites ceramic samples reveals that grain presence, there is some melting in the phase grain boundary, which may be due to the long-term high temperature affecting the $LaTiO_3$ phase. However, when the doping Mg^{2+} amount x=0.9 (Fig. 10c), the melt phenomenon does not appear, which embodies the advantage of doping Mg^{2+}. Based on the above analysis of density and SEM images, ceramics prepared by using solid-state reaction method are denser; the ion distribution is more uniform, and configurations more stable. For air aging of $La_{1-x}Mg_xTiO_3$ (x=0.1, 0.3, 0.5, 0.7, 0.9) NTC composites ceramic samples there will be an oxidation starting from the grain boundaries which results in the formation of cationic vacancies. At sufficient high temperatures at 1100 °C that these vacancies can diffuse into the grain.

The result is a NTC ceramic with a high cationic vacancy concentration and a non-ideal distribution of cations and cationic vacancies, thus the $La_{1-x}Mg_xTiO_3$ (x=0.1, 0.3, 0.5, 0.7, 0.9) NTC samples composites ceramic will be unstable with respect to aging. After prolonged aging about 800 h the cationic vacancies will be distributed homogeneously over the ceramics. Furthermore, the cations and cationic vacancies migrate to their ideal site. Consequently after the aging test, the ceramics reach a state in which they are stable. The aging improvement can also be explained by the change of Ti^{4+} ions distribution, and the dense ceramic structures. In the present study, the ion reaction $Ti^{4+} - \sigma Ti^{4+} \rightarrow (1-\sigma)Ti^{4+} + \sigma Ti^{3+} - \sigma e^-$ is also verified by the XPS analysis on $La_{1-x}Mg_xTiO_3$ NTC composites ceramic samples. It can be seen clearly that aging at 1100 °C has led to a significant decrease in the number of Ti^{4+} ions and to an increase in the number of Ti^{3+} ions [Table 2 Ti^{3+}/Ti^{4+} (aging)] area ratios for the $La_{0.5}Mg_{0.5}TiO_3$, $La_{0.3}Mg_{0.7}TiO_3$ and $La_{0.1}Mg_{0.9}TiO_3$

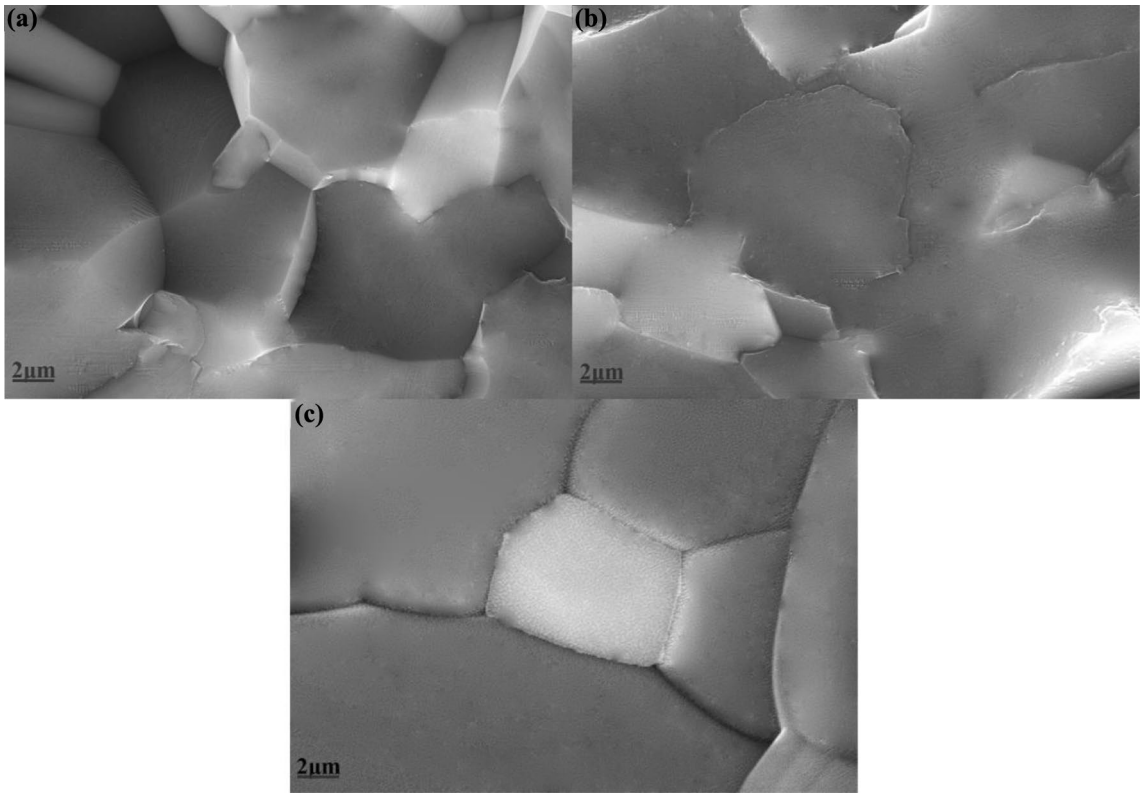

Fig. 10 SEM of fracture of $La_{1-x}Mg_xTiO_3$ NTC composites ceramic samples aging 800 h (aging at 1100 °C): **a** $x=0.5$, **b** $x=0.7$, and **c** $x=0.9$

are 1.4877, 6.3528 and 15.5168, respectively. These changes in the valence will affect the electrical properties of the materials. In addition, higher Mg^{2+} content at the grain boundary region is favorable for ceramic densification.

4 Conclusions

The $MgTiO_3$ and $LaTiO_3$ composites perovskite NTC ceramics materials have been prepared successfully by solid-state reaction method. XRD patterns of the samples $La_{1-x}Mg_xTiO_3$ ($x=0.1$, 0.3, 0.5, 0.7, 0.9) composites ceramic sintered at 1400 °C, prove the double perovskites consist of the $LaTiO_3$ phase and the $MgTiO_3$ phase. Through the XPS analysis, the co-existing of Ti^{3+}/Ti^{4+} is confirmed, which are proposed to be the intrinsic conduction mechanism for its NTC properties. Electrical measurements indicate that the electrical resistivity increases remarkably from 14,693.137 to 65,659.809 Ω cm with the increase of Mg^{2+} content, whereas the thermal constant $B_{400/1200}$ increases from 7785.270 to 24,948.100 K. It is suggested from the aging phenomenon that the resistance almost does not change with Mg^{2+} ion doped when the aging time is from 500 to 800 h due to the cation vacancies and ions migration. Doped Mg^{2+} in $LaTiO_3$ make the electrical stability of composite NTC thermistors have better than electrical stability ($\Delta R/R_0=0.1\%$ when $x=0.9$) in comparison with the Mg^{2+} few thermistors ($\Delta R/R_0=2.01\%$ when $x=0.1$). It is concluded that the $La_{1-x}Mg_xTiO_3$ ($x=0.1$, 0.3, 0.5, 0.7, 0.9) composites ceramic with $MgTiO_3$ and $LaTiO_3$ composites are useful for industrial applications as NTC thermistors over a 400–1200 °C wide temperature range.

Acknowledgements This study was supported by the Tianshan Cedar Project of Xinjiang Uygur Autonomous Region (Grant No. 2018XS09), National Natural Science Foundation of China (Grant No. 51872326), Xinjiang Key Laboratory Foundation (Grant No. 2018D04006) and Xinjiang Tianshan Talent Project.

References

1. C.J. Ma, Y.F. Liu, Y.N. Lu, J. Mater. Sci. Mater. Electron. **26**, 7238 (2015)
2. D.L. Fang, Z.B. Wang, P.H. Yang, W. Liu, C.S. Chen, A. Winnubst, J. Am. Ceram Soc. **89**, 230 (2006)
3. J. Ryu, K.Y. Kim, J.J. Choi, B.D. Hahn, W.H. Yoon, B.K. Lee, J. Am. Ceram. Soc. **92**, 3084 (2009)
4. K. Park, J. Am. Ceram. Soc. **88**, 862 (2005)
5. L.L. He, Z.Y. Ling, J. Appl. Phys. **110**, 093708 (2011)
6. D. Houivet, J. Bernard, J.M. Haussonne, J. Eur. Ceram. Soc. **24**, 1237 (2004)
7. C. Yuan, T. Yang, G. Chen, C. Zhou, Y. Yang, X. Zhou, Int. J. Appl. Ceram. Technol. **12**, 235 (2016)
8. G.H. Jonker, J.H. Van, Santen. J. Phys. A **16**, 337 (1950)

9. E.O. Wollan, W.C. Loehler, J. Phys. Rev. **100**, 545 (1995)
10. C.H. Hou, Z.H. Qian, J. Phys. Conf. Ser. **263**, 012 (2011)
11. R.A. Souza, J.A. Kilner, J. Solid State Ion. **106**, 175 (1998)
12. J.H. Kim, Y.M. Park, J. Power Sources **196**, 3544 (2011)
13. D.K. Hwang, S. Kim, J.H. Lee, J. Mater. Chem. **21**, 1959 (2011)
14. T. Ueda, U. Mitsunori, O. Hajime, J. Ion. **18**, 1 (2010)
15. Z.X. Xiong, J. Pan, H. Xue, M.F. Mai, H. Qiu, L.F. Chen, J. Ferroelectr. **408**, 86 (2010)
16. M. Khalid, M. Shuaib, A. Khan, Key Eng. Mater. **442**, 422 (2010)
17. R.J.H. Voorboeve, J.P. Pemeika, P.E. Freeland, J. Sci. **177**, 353 (1972)
18. H. Aria, T. Yamada, K. Eguchi, J. Appl. Catal. **26**, 265 (1986)
19. K. Fujishima, Honda. Nature **238**, 353 (1972)
20. J.H. Carey, Bull. Environ. Contam. Toxicol. **16**, 697 (1976)
21. S. Lei, H.Q. Fan, X.H. Ren, J. Mater. Chem. C **5**, 4040 (2017)
22. J. Sui, H.Q. Fan, B. Hu, Ceram. Int. **45**, 20427 (2019)
23. W. Chen, H. Fan, C. Long, S. Lei, J. Mater. Sci. Mater. Electron. **25**, 1505 (2014)
24. S.M. Ke, H.T. Huang, H.Q. Fan, J. Solid State Ion. **179**, 1632 (2008)
25. M. An, H.M. Zhang, Y.K. Weng, Front. Phys. **11**, 83 (2015)
26. D. Fasquelle, J.C. Carru, L.L. Gendre, C.L. Paven, J. Pinel, F. Chevire, F. Tessier, J. Eur. Ceram. Soc. **25**, 2085 (2005)
27. M. Kimura, S. Nanamatsu, K. Doi, Jpn. J. Appl. Phys. **11**, 904 (1972)
28. M. Bradha, S. Hussain, S. Chakravarty, J. Ion. **20**, 1343 (2014)
29. L. Zhang, Appl. Catal. B **33**, 418 (2012)
30. C.L. Paven, Y. Lu, H.V. Nguyen, Thin Solid Films **553**, 76 (2014)
31. S. Kim, W.H. Jung, Y. Inaguma, T. Nakamura, M. Ioth, Mater. Res. Bull. **3**, 307 (1995)
32. R. Osborn, M.C. Aronson, J.E. Greedan, J. Appl. Phys. **79**, 6432 (1996)
33. Y.W. Kim, D.P. Kwon, J. Norton, Solid State Electron. **12**, 2177 (2003)
34. K. Park, I.H. Han, J. Electroceram. **17**, 1079 (2006)
35. Y. Xin, L. Xu, J. Wang, X. Li, Rare Met. Mater. Eng. **39**, 1903 (2010)
36. E. Walle, A. Borg, E.M. Johansson, J. Phys. Chem. **115**, 9545 (2011)